

Investigation of the Wave Field Around a Monopile Due to Long Crested Irregular Waves in Moderate Steepness

Ivandito Herdayanditya^{1, 2}, Maximilian Streicher³, Evert Lataire⁴, and Pieter Rauwoens⁵

Abstract

Monopile foundations are the most built foundations in the offshore wind industry. The diameter is also expected to increase in the near future to accommodate larger wind turbines in deeper water depths. The large monopile diameter imposes additional challenges in planning marine operations near the monopile, as the monopile can no longer be treated as a transparent monopile. Therefore, proper wave field estimation around the monopile that also accounts for the monopile existence is needed to assure the safety of the operations. An investigation of the wave field around a monopile due to long crested irregular incident waves is provided in the present study. An experimental study was performed with different irregular wave properties, varying the wave steepness and the wave diffraction number. The present study extends the available experimental studies that focus primarily on the runup of the monopile. Initially, Linear Transfer Functions (LTFs) of the wave field around a monopile from the experimental study were compared to the linear theory and found to match well in the high energy frequency range. Small linear coherances are also seen in the low and high frequency ranges, indicating pronounced nonlinear effects in those frequency ranges. Further, the elevation time series is investigated via exceedance probability analysis and significant value computation. It is found that the crest exceedance probability of the wave field around a monopile does not correspond to the linear theory, while the wave height exceedance probability can be predicted well using the linear theory. Moreover, Wave Type II, which travels in the clockwise/anti-clockwise direction around a monopile and not in the radial direction, influences the crest properties.

Keywords:

Waves, monopile, marine operations, diffraction

¹ivandito.herdayanditya@kuleuven.be; Department of Civil Engineering, KU Leuven, Bruges, Belgium
²ivandito.herdayanditya@ugent.be; Ships and Marine Technology, Ghent University, Belgium
³maximilian.streicher@ugent.be; Department of Civil Engineering, Ghent University, Belgium
⁴evert.lataire@ugent.be; Ships and Marine Technology, Ghent University, Belgium
⁵pieter.rauwoens@kuleuven.be; Department of Civil Engineering, KU Leuven, Bruges, Belgium


Research Article. **Submitted:** 10 May 2024. **Reviewed:** 28 November 2024. **Accepted** after double-blind review: 20 December 2024. **Published:** 28 December 2024.

DOI: [10.59490/jchs.2024.0039](https://doi.org/10.59490/jchs.2024.0039)

Cite as: Herdayanditya, I., Streicher, M., Lataire, E., Rauwoens, P., Investigation of the Wave Field Around a Monopile Due to Long Crested Irregular Waves in Moderate Steepness, Journal of Coastal and Hydraulic Structures, 39, DOI: 10.59490/jchs.2024.0039

This paper is part of the **Thematic Series** of selected papers on advances in physical modelling and measurement of Coastal Engineering issues, as presented on the Coastlab Conference in Delft in 2024.



The Journal of Coastal and Hydraulic Structures is a community-based, free, and open access journal for the dissemination of high-quality knowledge on the engineering science of coastal and hydraulic structures. This paper has been written and reviewed with care. However, the authors and the journal do not accept any liability which might arise from use of its contents. Copyright © 2024 by the authors. This journal paper is published under a CC BY 4.0 license, which allows anyone to redistribute, mix and adapt, as long as credit is given to the authors. 

1 Introduction

Climate change has brought the need to rely more on affordable and clean energy, as mentioned in one of the Sustainable Development Goals (UN, 2015). Among various renewable energy sources, offshore wind energy has been explored and exploited substantially, giving notable growth in the last decade ($\approx 36\%$) (GWEC, 2023). Oil and gas offshore structures, such as monopiles, jackets, and gravity-based foundations, are adapted to support wind turbines in the coastal or offshore environment. Notably, monopiles have become the most built offshore wind turbine foundations (Ramirez et al., 2020). The diameter of the offshore wind monopiles has also increased recently to extend its capability to operate with higher wind turbine rated power in the intermediate water depth, going from a typical monopile radius of 5 – 7 m for ≈ 3 MW wind turbines (Negro et al., 2017) into the monopile radius of 10 m for 15 MW wind turbines (Gaertner et al., 2020).

Safe marine operations close to a monopile require proper estimation of the Wave Field Around a Monopile (WFAM). MacCamy and Fuchs (1954) derived an analytical solution for the regular WFAM, employing potential flow and free surface linearisation. Consequently, the linear solution underestimates regular WFAM experiments in the moderate to high steepness incident waves (Kriebel, 1992; Morris-Thomas and Thiagarajan, 2004). Further, nonlinear analytical solutions have been studied to address the underestimation (Kriebel, 1990; Chau and Taylor, 1992; Molin et al., 1995). The linear regular WFAM solution is also utilised to estimate the WFAM from irregular incident waves, introducing Linear Transfer Functions (LTFs). The LTF method manages to capture the runup spectrum (i.e. the WFAM spectrum at the surface of the monopile) (Niedzwecki and Duggal, 1992; Wang and Low, 2019).

A comparison between input and output time series can extract the LTFs and Quadratic Transfer Functions (QTFs) (Kim, 2008). The LTF and the QTF can be used to construct an input-output model through a Volterra Quadratic Model, having been used for e.g. ship added resistance problems (Dalzell, 1976), moored structures (Kim and Kim, 2005), or runup on a mini Tension Leg Platform (TLP) (Sibetheros et al., 2005). There are also linear and quadratic coherances to quantify the significance of the LTF and the QTF contributions. Herdayanditya et al. (2024b) performed a comparison analysis between the incident waves and WFAM time series, finding that the LTF is applicable between $0.75f_p - 1.75f_p$, where f_p (Hz) is the peak frequency of the incident wave spectrum. Outside that range, nonlinear interactions between the incident waves and the WFAM are more pronounced. The finding in Herdayanditya et al. (2024b), employing low diffraction number monopile, is similar to Sibetheros et al. (2005) despite the difference in modelled structures: a monopile and a Tension Leg Platform (TLP). Furthermore, the nonlinear irregular WFAM is also studied by Wang and Low (2019) via semi-analytical solutions, concluding that nonlinearity has a negligible effect on the spectral estimation but is important for the extreme value estimation.

Numerical simulations are also employed to study the WFAM, making it easier to solve complex cases, such as multi body simulations between a monopile and an operation vessel. Herdayanditya et al. (2024a) demonstrated the need to account for the operation vessel to estimate the WFAM in the monopile-vessel situation where the findings are deduced from a linear potential flow solver, Capytaine (Ancellin and Dias, 2019; Babarit and Delhommeau, 2015). The WFAM nonlinear properties can also be obtained with numerical simulations, solving either Fully Nonlinear Potential Flow (Ferrant et al., 1999; Büchmann et al., 1999; Lin et al., 2021) or Navier-Stokes equations (Liu et al., 2019; Jiang and el Moctar, 2022; Herdayanditya et al., 2022). However, it should be noted that high-fidelity numerical tools might not be suitable for marine operational needs where the computational cost of the tools is considerably expensive. For instance, Herdayanditya et al. (2022) observed a computational time of around 50 minutes for 1 second simulated time of only regular waves around a monopile in Lagrangian and Eulerian Incompressible Navier-Stokes simulations. Meanwhile, the operational limit is usually investigated with the irregular waves assumption and in the nature of rapid decision-making situations.

$$\zeta_C = \alpha\eta_C + \beta\frac{u_\eta^2}{2g} \quad (1)$$

Empirical equations have also been studied to provide fast estimation of the WFAM, although it is limited to the maximum wave runup, ζ_C (m), around a monopile, as in Eq. (1). The α and β in Eq. (1) are the dimensionless empirical constants giving the relationship between the incident wave crest, η_C (m), the water velocity, u_η (m/s), and the gravity acceleration, g (m/s²). It comes from the stagnation point condition derived with Bernoulli equation; $\alpha = 1$ and $\beta = 1$ (Hallermeier, 1976). Further, α and β are tuned empirically from a set of experiments (Niedzwecki and Duggal, 1992). De Vos et al. (2007) observed new empirical coefficients of α and β by considering u_η of the Stoke's second order theory rather than the linear theory, giving better estimations of their experiment results. Moreover, Andersen et al. (2011) reanalysed the data and applied the stream function to estimate the velocity and split the coefficients into low and high steepness cases. This approach also gives satisfactory results for wave runups in breaking wave conditions (Ramirez et al., 2013). Although the empirical estimation excels in estimating the maximum wave runup around a

monopile, it misses the WFAM information in various radial and angular positions around the monopile.

The present research investigates the WFAM from irregular incident waves with moderate steepness via physical experiments. The incident wave steepness is limited to the moderate steepness condition considering that the research interest lays within the marine operational limits in the offshore wind farm. Thus, high nonlinear waves or breaking incident waves are outside of the scope in this study. Section 2 provides the theoretical background needed to assess the experiment campaigns. It contains the analytical solution of the WFAM, post processing method to extract the LTF, and time series analysis method. Afterwards, in Section 3, the physical experiment cases and procedures are given, extending the study cases given in Herdayanditya et al. (2024b). The LTF and Exceedance Probability discussion are given in Section 4 and Section 5. Additionally, significant value of the WFAM is also discussed in Section 6. Finally, the conclusion is drawn up in Section 7.

2 Wave Field Around a Monopile

2.1 Linear Potential Theory

Potential flow theory, within the inviscid, irrotational, and incompressible fluid assumptions, is employed to calculate the WFAM. Free surface linearisation is also applied to the free surface boundary condition, giving the analytical solution of the linear regular WFAM, shown in Eq. (2) (MacCamy and Fuchs, 1954; Kriebel, 1990). Eq. (2) computes the WFAM complex amplitude, ζ_o (m), for a monopile with radius, R (m), at a radial position, r (m), and an angular position, θ (rad), where H_η (m) is the incident regular wave height, $\epsilon_n = 1$ if $n = 0$, else $\epsilon_n = 2i^{-n}$, $J_n(kr)$ is the Bessel function of the first kind, and $H_n(kr)$ is the Henkel function. The wave number, k (rad/m), is related to the wave angular frequency, ω (rad/s), along with the water depth, h (m), and the gravity acceleration, g (m/s²), via dispersion relation, Eq. (3). Thus, different incident regular waves properties induce different WFAM properties.

$$\zeta_o(r, \theta) = \frac{H_\eta}{2} \sum_{n=0}^{\infty} \epsilon_n \left[J_n(kr) - \frac{J'_n(kR)}{H'_n(kR)} H_n(kr) \right] \cos(n\theta) \quad (2)$$

The absolute magnitude of the complex amplitude, $|\zeta_o(r, \theta)|$, gives the amplitude of the WFAM, while the arctan (ζ_o) gives the phase of the WFAM with units of meter and radians respectively. Thus, the WFAM time series can be constructed as Eq. (4), where t (s) is the time. It has to be noted that the linear regular WFAM also assumes linear incident waves where the time series of the water elevation is $\eta(x, y, t) = \mathbb{R} \left\{ \frac{H_\eta}{2} \exp [i(kx \cos \psi + ky \sin \psi)] \exp [i(-\omega t + \phi_\eta)] \right\}$ in which x, y (m) are the cartesian position, ψ (rad) is the incident wave direction, and ϕ_η (rad) is the incident wave phase. The unit of $\eta(x, y, t)$ is meter.

$$\omega^2 = gk \tanh kh \quad (3)$$

$$\zeta(r, \theta, t) = \mathbb{R} \{ \zeta_o(r, \theta) \exp(-i\omega t) \} \quad (4)$$

2.2 Linear Transfer Function

The linear irregular WFAM can be constructed as the superposition of the regular WFAM from Eq. (4) accounting for multiple ω_j and $\zeta_{o,j}$ as shown in Eq. (5). The multiple incident wave components (H_{η_j} and ϕ_{η_j}) can be computed from the incident spectrum, $S_\eta(f)$ (m²/Hz), where $H_{\eta_j} = 2\sqrt{2S(f_j)\Delta f_j}$, and ϕ_{η_j} is randomly selected. f (Hz) is the wave frequency where it is related to the wave angular frequency as $\omega = 2\pi f$. Since this study is limited to the long-crested waves, ψ_j of the incident waves is assumed to be 0 and there is no directional spectrum introduced. The WFAM in short-crested waves can also be derived in the same manner including the directional components as explained in Ji et al. (2017). From Eq. (5) the WFAM statistics can be deduced (e.g. significant height of the WFAM, H_{s_ζ} (m)).

$$\zeta(r, \theta, t) = \mathbb{R} \left\{ \sum_{j=1}^N \zeta_{o,j}(r, \theta) \exp(-i\omega_j t) \right\} \quad (5)$$

The WFAM statistics can also be estimated via frequency domain analysis rather than constructing the time domain simulation of Eq. (5). The WFAM spectrum, $S_\zeta(f)$ (m^2/Hz), is computed according to Eq. (6) (Niedzwecki and Duggal, 1992), utilising $S_\eta(f)$ and the WFAM Linear Transfer Function, $\text{LTF}(f)$ (m/m). LTF is also sometimes referred as Response Amplitude Operators (RAO) in the context of seakeeping analysis. There are various $S_\eta(f)$ models where JONSWAP spectrum is applied in this study. Eq. (7a) shows the JONSWAP spectrum in a function of ω thus $S(f) = 2\pi S(\omega)$ where a and α are computed with Eq. (7b) and Eq. (7c). $\epsilon_S = 0.07$ when $\omega \leq \omega_p$ else $\epsilon_S = 0.09$. The JONSWAP spectrum requires information of the significant incident wave height, $H_{s\eta}$ (m), the peak period, $T_p = \frac{2\pi}{\omega_p}$ (s), and the peak enhancement factor, γ . Meanwhile, the LTF is the ratio between the regular WFAM height, H_ζ (m), and the incident regular wave height, H_η (m), computed as in Eq. (8). H_ζ can also be written as twice of the WFAM amplitude, ζ_o (m). The LTF computation employs Eq. (2) in various incident wave frequencies, resulting theoretical $\text{LTF}(f)$ as a function of wave frequencies. The LTF also characterises the WFAM for a particular monopile because different monopile R , and different h , would derive different LTFs. Moreover, the LTF provides generalised solution of the WFAM in various locations so that it is not limited to the runup around the monopile. The computation cost is also minimal, suitable for marine operation planning needs.

$$S_\zeta(f) = \text{LTF}^2(f)S_\eta(f) \quad (6)$$

$$S_\eta(\omega) = \frac{5}{16} H_{s\eta}^2 \omega_p^4 \omega^{-5} \exp \left[-\frac{5}{4} \left(\frac{\omega}{\omega_p} \right)^{-4} \right] \gamma^a \alpha(\gamma) \quad (7a)$$

$$a = \exp \left[-\frac{1}{2} \left(\frac{\omega - \omega_p}{\epsilon_S \omega_p} \right)^2 \right] \quad (7b)$$

$$\alpha(\gamma) = 1 - 0.287 \ln(\gamma) \quad (7c)$$

$$\text{LTF}(r, \theta) = \frac{H_\zeta}{H_\eta} = \frac{2\zeta_o(r, \theta)}{H_\eta} \quad (8)$$

While the analytical LTF is available a priori, the physical experiment LTF is computed from the irregular incident waves, $\eta(t)$ (m), and the irregular WFAM, $\zeta(t)$ (m), time series. Utilizing Fast Fourier Transform (FFT) analysis, the FFT complex amplitude of the irregular incident waves and the WFAM time series, in meter, are $P(f)$ and $Q(f)$ respectively. Afterwards, $P(f)$ and $Q(f)$ are utilised for the LTF computation in Eq. (9). $E[PQ^*]$ refers to the cross density spectrum between the incident waves and the WFAM while $E[|P|^2]$ refers to the incident waves density spectrum. Linearity between the two signals can also be assessed with dimensionless linear coherence (Coh.) as in Eq. (10). The value of coherence is $0 \leq \text{Coh.} \leq 1$, one refers to fully linear relationship and zero means fully nonlinear relationship. The present study is limited to the LTF evaluation, thus the QTF and the higher-order coherence are not discussed.

$$\text{LTF} = \frac{E[PQ^*]}{E[|P|^2]} \quad (9)$$

$$\text{Coh.} = \frac{E[(PQ)^2]}{E[|P|^2] E[|Q|^2]} \quad (10)$$

2.3 Time Series Assessment

Zero up-crossing components are assessed for the time series evaluation. Within each up-crossing wave component, l , the maximum elevation (crest), ζ_{C_l} (m), and the minimum elevation (trough), ζ_{T_l} (m), are recorded. The difference between ζ_{C_l} and ζ_{T_l} is identified as wave height, being twice of the amplitude ($H_{C_l} = 2\zeta_{o_l}$, m). The present study focuses on ζ_C and H_{C_l} . To generalize the discussion, the two up-crossing parameters are identified as x , thus $x \in [2\zeta_C, H_\zeta]$ (m).

2.3.1 Exceedance Probability

Rayleigh distribution is employed as the theoretical estimation for wave height and crest exceedance probabilities, $P_E(x_p)$. The Rayleigh cumulative distribution function, seen as theoretical $F(x_p)$, quantifies the probability of occurrence for which x is under a specified threshold, x_p , i.e. $F(x_p) \equiv \Pr(x \leq x_p)$. Eq. (11) computes $F(x_p)$ where m_0 (m) is the zeroth moment that is computed from either $S_\eta(f)$ or $S_\zeta(f)$ in Eq. (6), computing $F(x_p)$ of either the incident waves or the WFAM. Meanwhile, the physical experimental $F(x_p)$ is computed by at first reordering the x_l in the increasing order so that $x_p < x_{p+1}$. By computing the number of sample x at below x_p , notated by n_{x_p} , the $F(x_p)$ of the experiment data can be computed with Eq. (12) where N is the total number of x records.

$$F_p(x_p) = 1 - e^{-\frac{x_p^2}{8m_0}} \quad (11)$$

$$F_p(x_p) = \frac{n_{x_p}}{N} \quad (12)$$

From the theoretical and experimental $F(x_p)$, theoretical and experimental exceedance probability, $P_E(x_p)$, can be obtained. Eq. (13) computes $P_E(x_p)$, considering that $P_E(x_p) \equiv \Pr(x \geq x_p)$. It describes the probability of x being larger than x_p . Furthermore, exceedance probabilities assuming nonlinear waves have also been studied to account for the crest exceedance of the ocean waves (i.e. without monopile in place). Nonlinear crest exceedance probability from Forristall (2000) and Gramstad and Lian (2024) are utilised for the nonlinear crest distribution, described in Appendix A.

$$P_E(x_p) = 1 - F_p(x_p) \quad (13)$$

2.3.2 Significant Value

The x_p list from the experimental records is employed to obtain the significant value of x . The significant value is defined as the average of the largest one-third of x_p , Eq. (14). The time series significant value from the experiments is compared to the theoretical significant value which is computed with the spectra analysis. The theoretical significant value of the WFAM height and the WFAM crest are computed with Eq. (15a) and Eq. (15b) respectively, where $m_{0\zeta}$ is the zeroth moment of $S_\zeta(f)$.

$$x_s = \frac{\sum_{p=\frac{2}{3}N}^N x_p}{\frac{1}{3}N} \quad (14)$$

$$H_{s\zeta} = 4\sqrt{m_{0\zeta}} \quad (15a)$$

$$\zeta_{Cs} = 2\sqrt{m_{0\zeta}} \quad (15b)$$

3 Experiment Set-Up

The Coastal & Ocean Basin (COB) in Ostend, Belgium, was utilised to perform the experiment campaigns. The wave tank dimension is 30 m \times 30 m with 20 m \times 20 m L-shaped wave makers and absorber beaches on the other two sides (Figure 1). The wave makers are also able to perform active absorption beside generating the waves. A monopile was placed at coordinates $x = 8400$ mm, $y = 13400$ mm (see Figure 1) in the basin. From a series of regular wave tests without the monopile in place, it was concluded that at this location, unwanted waves (e.g. diffraction effect from the short guiding wall near the rear end of the east wave maker) and dissipation effects from the north side passive absorber were minimized, ensuring optimal wave quality at the measurement location. It has to be noted that different guiding wall arrangement would consequently result in different optimised location. During the campaign, only east wave maker was activated to generate the waves while the south wave maker only acted as an active wave absorber and a guiding wall. Resistance wave gauges were utilised to measure the free surface elevation with measurement rate of 40 Hz.

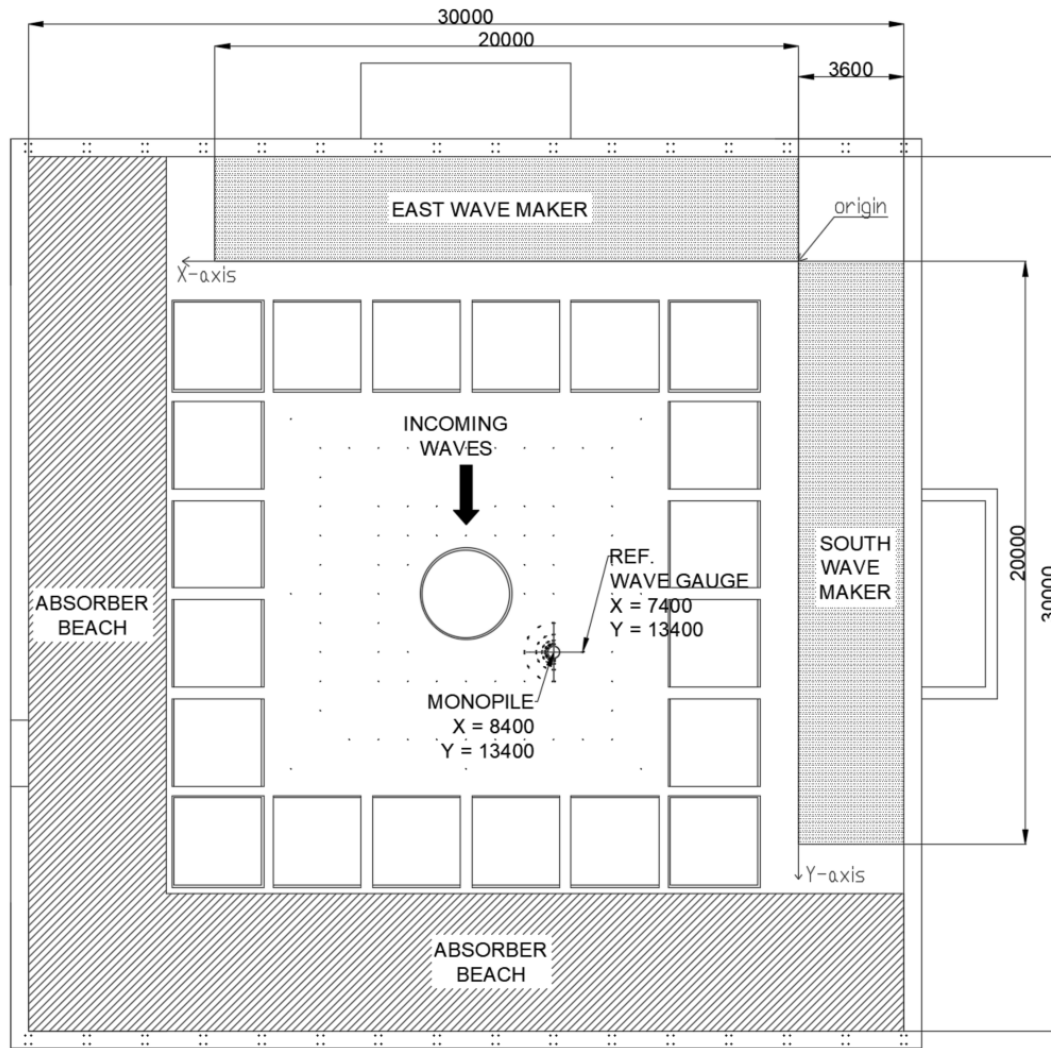


Figure 1: Experimental set up scheme of the monopile location during the experiments in the Coastal & Ocean basin (COB). The wave basin consists of wave makers along the east and south sides and wave absorbing beaches along the north and west sides. All units are given in mm.

Table 1: Irregular wave parameters for the experimental campaign. The wave properties in the model are scaled by the Froude's length scale, $w = 25$ and the Froude's time scale, $\sqrt{w} = 5$.

	Model		Full Scale	
	T_p (s)	$H_{s\eta}$ (m)	T_p (s)	$H_{s\eta}$ (m)
Wave 1		0.037		0.93
Wave 2	1.00	0.050	5.00	1.25
Wave 3		0.075		1.88
Wave 4		0.10		2.51
Wave 5	1.67	0.13	8.35	3.35
Wave 6		0.20		5.02

3.1 Test Cases

A monopile with 10 m diameter, expected for 15 MW wind turbine, was taken as the monopile reference (Gaertner et al., 2020). The experiment Froude's length scale is 1:25, i.e. $w = 25$. Hence, the model diameter was 0.4 m. The wave tank water depth was 1.4 m which mimicked the 35 m water depth. Six long crested irregular waves were generated with two peak periods, T_p , where in each T_p (s), the wave steepness, $\frac{1}{2}k_p H_{s\eta}$, is varied. Table 1 shows the model and full scale wave parameters, identified by Wave 1 - Wave 6. The full scale and model wave properties are related by Froude's law. According to the Froude's law, the ratio between the full scale wave height and the model

Table 2: Nondimensional parameters in the wave monopile experiments

	Diffraction Number $k_p R$	Dispersity $k_p h$	Steepness $\frac{1}{2} k_p H_{s\eta}$
Wave 1			0.075
Wave 2	0.82	5.75	0.10
Wave 3			0.15
Wave 4			0.075
Wave 5	0.30	2.09	0.10
Wave 6			0.15

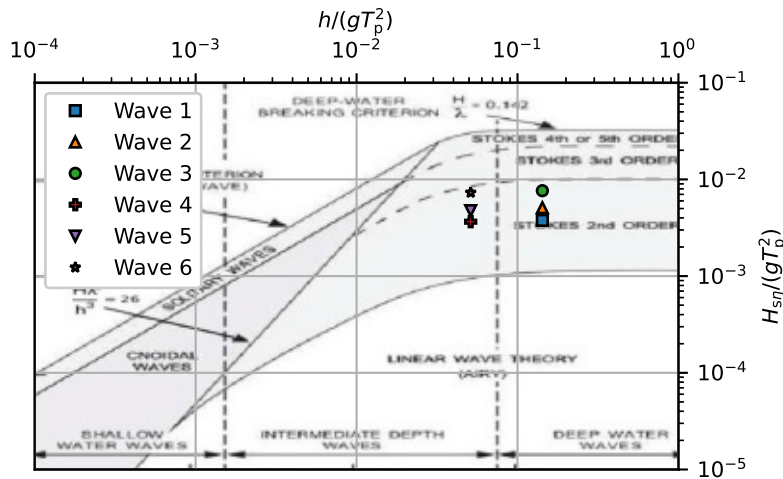


Figure 2: Wave case properties plotted in the Le Méhauté diagram.

wave height is w while the ratio between the full scale wave period and the model wave period is \sqrt{w} . The full scale properties provide the typical limiting wave conditions for marine operations. The irregular waves were generated with JONSWAP wave model, Eq. (7a), where the peak enhancement factor, γ , was 3.3. JONSWAP spectrum describes better the fetch-limited regions where the parameter is accounted for by γ . Meanwhile, the fully-developed waves (e.g. in the open ocean or areas facing the open ocean) can be described by Pierson-Moskowitz spectrum, equivalent to JONSWAP with $\gamma = 1$. Furthermore, the offshore wind turbines are also mostly built in the fetch limited area (e.g. Belgian Part of the North Sea), thus JONSWAP is more suitable to investigate the WFAM.

The nondimensional wave parameters, such as the wave steepness, the wave dispersity, and the diffraction number, are shown in Table 2. The steepness of the cases is within the moderate steepness $\frac{1}{2} k_p H_{s\eta} = 0.075 - 0.15$, where nonlinear effect is also expected. The wave dispersion suggests that the experiments were in the intermediate water depth ($\frac{\pi}{10} < k_p h < \pi$) and in the deep water depth ($k_p h > \pi$), while the diffraction number indicates that both effect of small and high diffraction force were taken into account. Despite the small diffraction number, disturbance of the waves is expected to be still observed around the monopile, as seen in the nonlinear regular waves runup (Kriebel, 1992). Furthermore, Figure 2 shows the wave properties location at the Le Méhauté diagram, from which H and T of the regular waves in the diagram are computed with $H_{s\eta}$ and T_p of the irregular waves, indicating Stoke’s second order wave domination in the present wave cases.

3.2 Experiment Procedure

3.2.1 Incident Wave Assessment

Initially, the irregular waves in the wave tank is assessed, employing the measurements of the reference wave gauge (WG) (Figure 1) without the monopile in place. The physical experiments aimed for ≈ 3 hours full scale time range, thus the reflection waves were inevitable. Utilizing the reflection decomposition method from Zelt and Skjelbreia (1992), the reflection coefficients in the wave tank $\approx 12\%$ in the wave frequencies. Figure 3 shows the measured incident wave spectrum compared to the theoretical JONSWAP spectrum. Qualitatively, the measured spectrum are

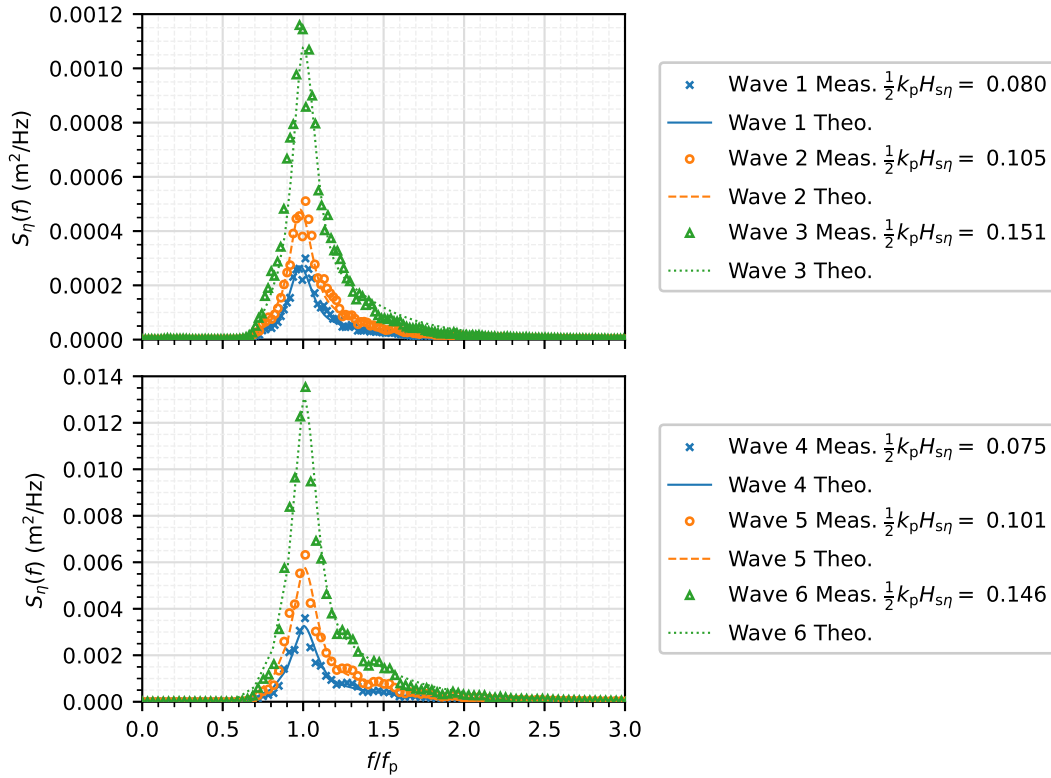


Figure 3: Comparison between the measured (Meas.) and theoretical (Theo.) incident wave spectrum, $S_\eta(f)$, for Wave 1 - Wave 6. The measured steepness $\frac{1}{2}k_p H_{s\eta}$ is also shown.

in good agreement with the JONSWAP model. Further, the measured steepness is computed to quantify the measured spectrum, which appears to be considerably similar to Table 2. k_p is computed with f_p employing Eq. (3). There is a post processing uncertainty in defining f_p where Young (1995) employed the weighting method with power of four to address the uncertainty, also applied in the present study. On the other hand, $H_{s\eta}$ is computed with $4\sqrt{m_{0\eta}}$ where $m_{0\eta}$ is the zeroth moment of the measured incident wave spectrum.

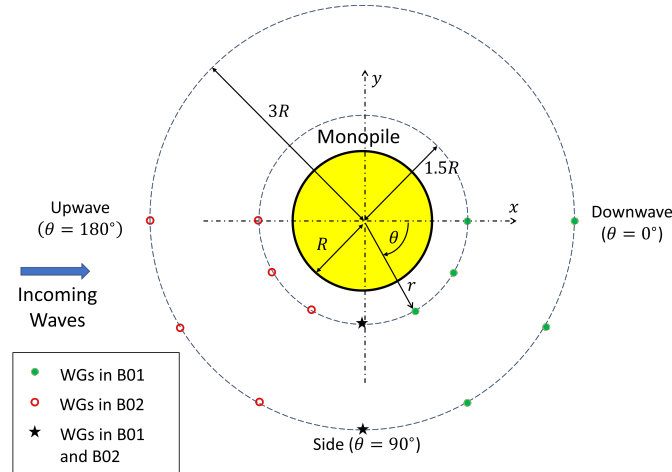
3.2.2 Wave Field around a Monopile

The reference WG and the monopile were installed side by side with two different WG arrangements namely B01 and B02 (Figure 4a). The WGs were placed at 5 radial positions and 7 angular positions in which only two radial positions are reported in this study, $r = [1.5R, 3R]$. B01 and B02 arrangements were employed to cover all the angular positions $\theta = [0^\circ, 30^\circ, 60^\circ, 90^\circ, 120^\circ, 150^\circ, 180^\circ]$ with limited number of WGs. Initially, the B01 arrangement was used to record all the wave cases in Table 1, covering $\theta = 0^\circ - 90^\circ$. Figure 4b shows the actual installation of the B01. Afterwards, the WGs were rotated into the B02 arrangement to measure the other angular positions. Meanwhile, the WGs at the $\theta = 90^\circ$ were kept in place as the check point between the B01 and B02.

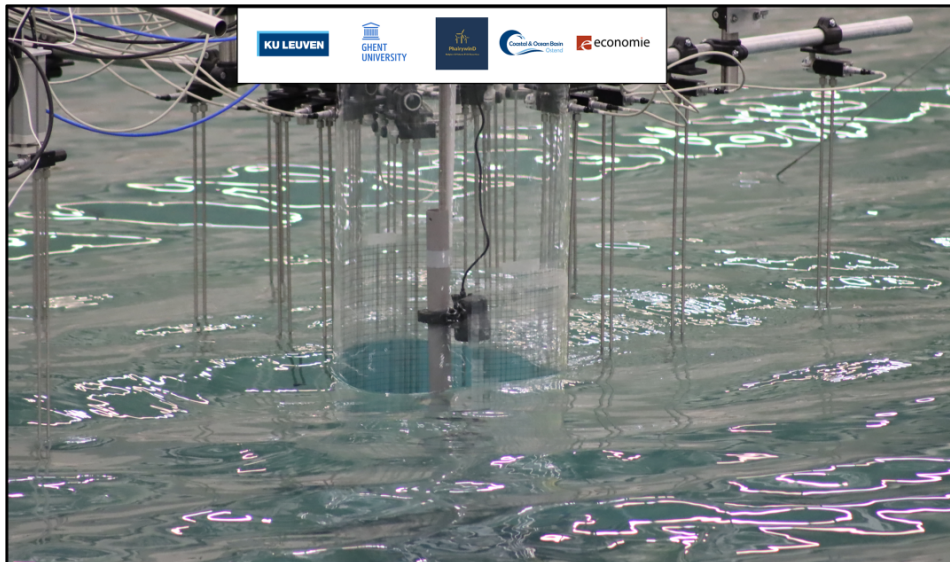
Comparisons of the WG measurement in the Wave 3 and Wave 6 at $\theta = 90^\circ$ between B01 and B02 are shown in Figure 5. The time series between the two measurements are almost identical, suggesting similar condition between B01 and B02, although there is a slight temporal shift in the Wave 6. Noticable shift also occurs in Wave 4 and Wave 5 with shifting of ≈ 0.25 s, but in Wave 1 - Wave 3. However, the time shift does not appear to affect significantly the LTF and the time series analysis exceedance probability analysis.

4 Transfer Function

$\eta(t)$ and $\zeta(t)$ from the experimental campaigns are utilised to compute the physical experimental LTF, Eq. (9), and the coherence, Eq. (10), at the various angular and radial positions. The physical experimental LTF is compared to the theoretical LTF, Eq. (8). The theoretical LTF does not vary in different steepness due to the linearisation. From the available WFAM locations, the upwave position ($\theta = 180^\circ$) from two T_p at $r/R = 1.5$ are shown in Figure 6. The



(a) B01 and B02 scheme for the Wave Gauges (WGs) arrangements during the experiments of irregular incident waves and monopile with radius R . The WG radial and angular positions are indicated by r and θ where the origin is at the center of the monopile.



(b) Actual condition of the wave gauges and the monopile in B01.

Figure 4: Wave gauge arrangements during the experiments.

frequency domain of the LTF and the coherence in Figure 6 can be split into three frequency ranges: 1. low frequency ($f/f_p < 0.75$), 2. wave frequency ($0.75 < f/f_p < 1.75$), 3. high frequency ($f/f_p > 1.75$). The splits are based on the significance of the incident wave energy.

The theoretical LTF in the first frequency range is unity ($LTF = 1$) indicating the monopile as a transparent structure. Nevertheless, the experimental LTF shows different value along with their low coherence values, as seen in Figure 6a and Figure 6b. Low coherence indicates that the experimental WFAM elevation in this frequency range does not linearly comes from the same frequency components. The experimental WFAM is most likely contributed from the interaction between two different wave frequencies from the wave frequency input range, possibly the difference-frequency interaction (Kim and Yue, 1990; Taylor and Huang, 1997; Wang and Low, 2019). Interestingly, the LTF at $f/f_p = 0$ also does not collapse to 1, suggesting that there is a change of mean value between the incident and the WFAM. The change of mean value of the WFAM is known in the regular wave cases, usually identified as the set-up or set-down of the the WFAM. In the regular waves, the set-up/set-down is contributed from the square of the first order potential (Kriebel, 1990).

In the wave frequency region, Figure 6a and Figure 6b show different characteristics. The high coherence ($Coh. > 0.85$) frequency range in Wave 1 - Wave 3 is smaller than in Wave 4 - Wave 6. In the latter cases, the high coherence extends up to $f/f_p = 1.75$. Therefore, the shorter peak period cases pronounce more nonlinearity. In this frequency range, the LTF estimation from the experiments correspond with the estimation of the linear potential flow, even in

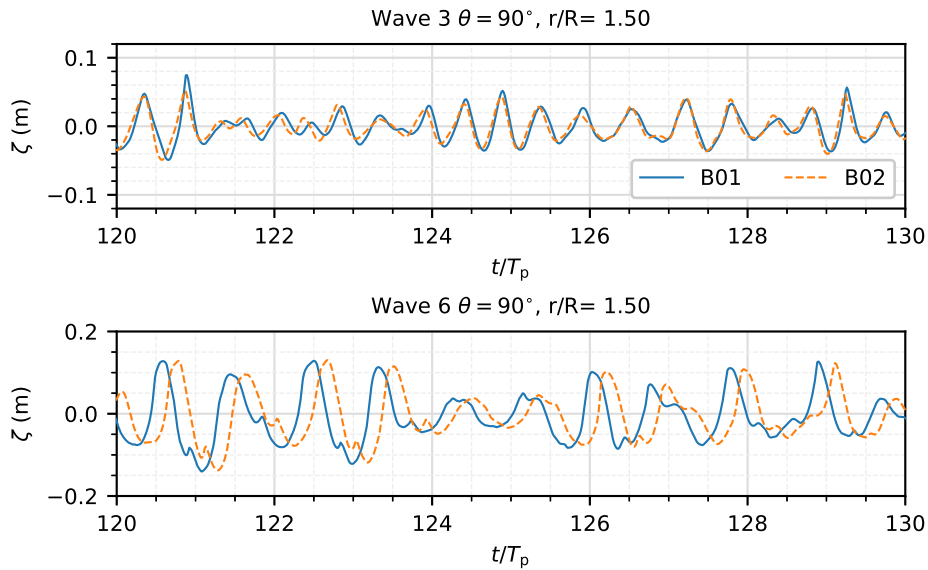
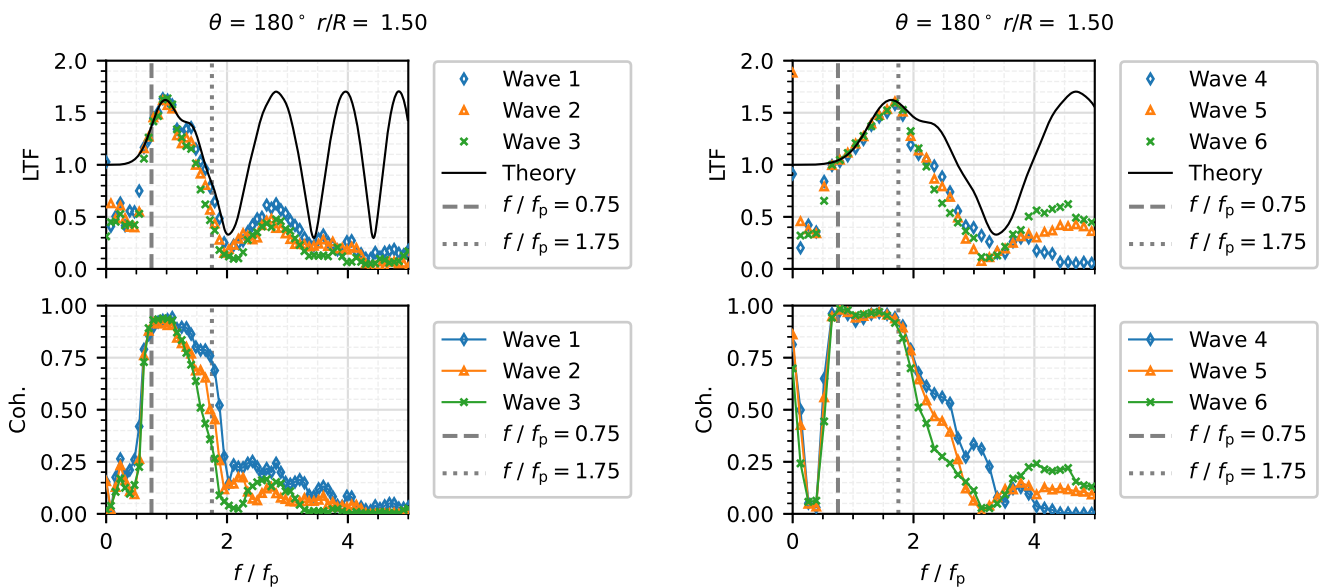


Figure 5: Comparison of the WG measurements of Wave 3 and Wave 6, featuring two different WGs layout (B01 and B02).



(a) LTF from Wave 1 - 3, with $T_p = 1.00$ s

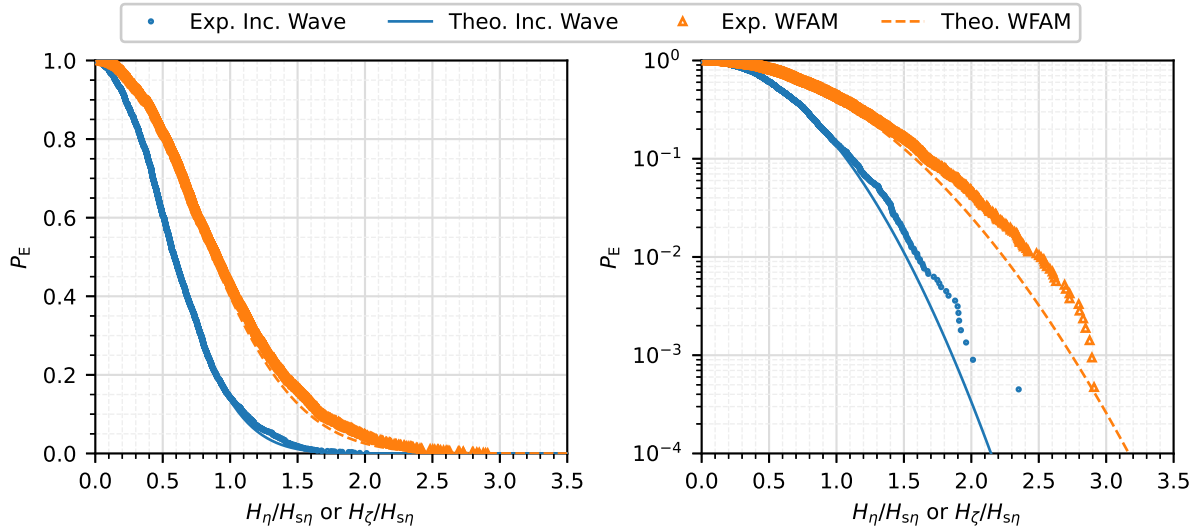
(b) LTF from Wave 4 - 6, with $T_p = 1.67$ s

Figure 6: Comparison of the Linear Transfer Function (LTF) and Coherence (Coh.) at the upwave $\theta = 0$, $r = 1.5R$ between the experiments and theoretical estimation.

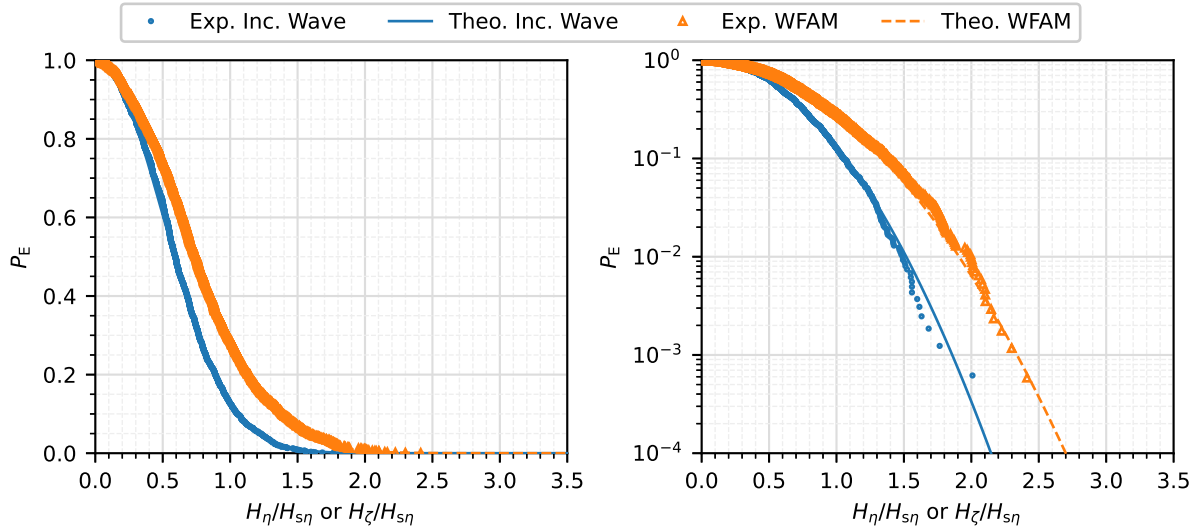
the increasing steepness cases. This suggests that the WFAM spectral analysis of the WFAM in linear or nonlinear computation methods provide similar results, similar to the findings of Wang and Low (2019).

In the last frequency range, the coherence changes in increasing steepness. The small steepness waves generally have higher value of coherence, indicating that the nonlinear effect is less pronounced than the high steepness incident waves. The nonlinear effects are due to the sum frequency interactions (Kim and Yue, 1990; Taylor and Huang, 1997; Wang and Low, 2019). It is also interesting to note that the theoretical LTF is also seen to oscillate in the high frequency. This is caused by the interaction between the incident and the diffracted waves creating a standing waves pattern in different frequency (Kriebel, 1990). Nevertheless, the experimental LTF does not correspond to the theoretical LTF in this frequency range.

The fact that the experimental LTF deviates from the theoretical LTF in the low and the high frequencies in the present study can be attributed to the numerical defects to estimate the LTF for the low amount of energy in the waves.



(a) P_E is computed with Wave 3 where $T_p = 1.00$ s and $H_s = 0.075$ m



(b) P_E is computed with Wave 6 where $T_p = 1.67$ s and $H_s = 0.20$ m

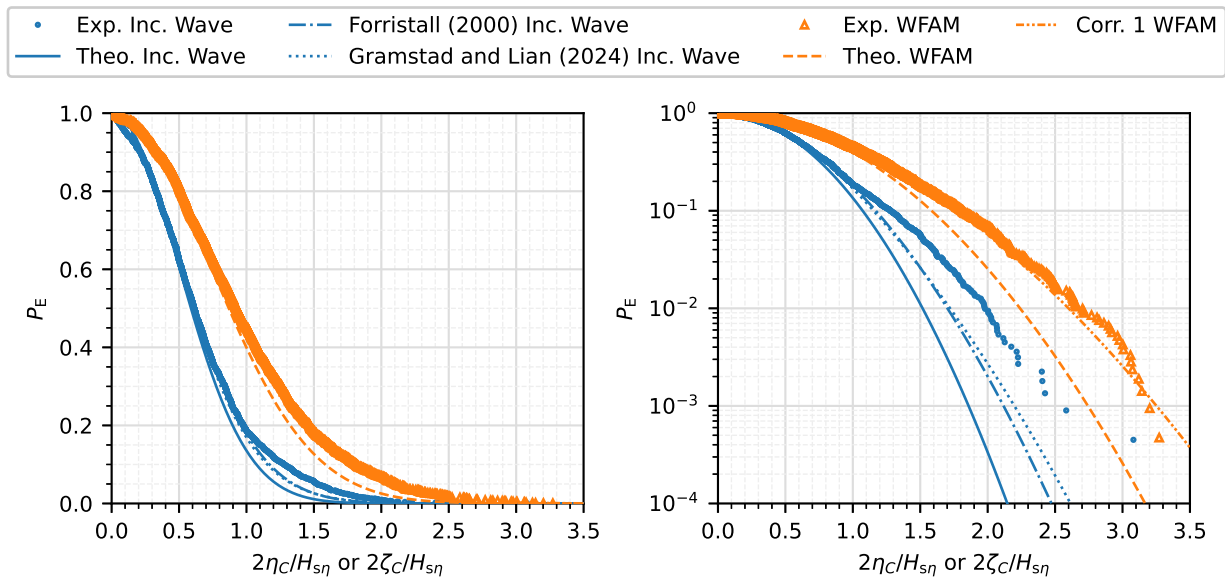
Figure 7: Comparison of the wave height exceedance probability, P_E , for the incident waves and the WFAM between the experiments and the linear theory at $\theta = 180^\circ$ and $r = 1.5R$, normalised with the incident significant wave height.

This can be elaborated from the wave frequency range of Figure 6a where the LTFs of Wave 1-3 at $f/f_p = 1.5 - 1.75$ still correspond to the theoretical LTFs, even though coherence values are small. This is mainly due to their sufficient amount of energy.

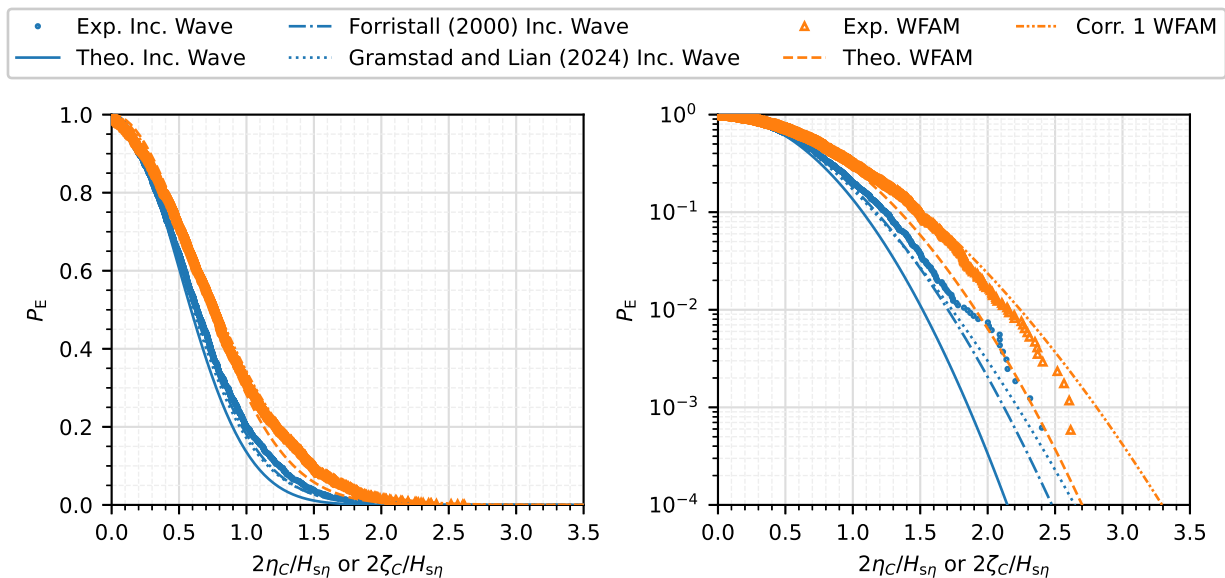
5 Exceedance Probability

At $\theta = 180^\circ$ and $r = 1.5R$, Wave 3 and Wave 6 are selected to identify the WFAM P_E . Besides, the incident waves P_E for Wave 3 and Wave 6 are also computed. Wave 3 and Wave 6 are selected as they are the most nonlinear cases in each T_p . P_E for both the incident waves and the WFAM are computed with Eq. (13). Figure 7 and Figure 8 show the wave height P_E and the crest P_E respectively for both the incident waves and the WFAM. The theoretical and experimental $F(x_p)$ are computed with Eq. (11) and Eq. (12) in turn. P_E in Figure 7 and Figure 8 is shown in two styles: 1. linear scale (left side) and 2. logarithmic scale (right side). The logarithmic scale is utilised to zoom in the low P_E while the high P_E is more visible in the linear scale.

For both T_p at the sampled position, the WFAM wave height P_E (Figure 7) and crest P_E (Figure 8) are higher



(a) P_E is computed with Wave 3 where $T_p = 1.00$ s and $H_s = 0.075$ m



(b) P_E is computed with Wave 6 where $T_p = 1.67$ s and $H_s = 0.20$ m

Figure 8: Comparison of the wave crest exceedance probability, P_E , for the incident waves and the WFAM between the experiments and the linear theory at $\theta = 180^\circ$ and $r = 1.5R$, normalised with the incident significant wave height. Corr. 1 applies the mathematical model of Forristall (2000) but the inputs are with WFAM spectral analysis.

than the incident waves. This can be correlated with the LTF of the sampled position (Figure 6), for which at the wave frequency range the LTF is more than one (i.e. amplification of the incident waves). The WFAM P_E being higher than the incident waves P_E is also observed from the theoretical P_E . Nevertheless, the theoretical P_E appears to perform differently between the wave height and crest estimations. The experimental wave height P_E is seen to be closer to the theoretical P_E than the experimental crest P_E to the theoretical crest P_E .

The wave height P_E of the experimental incident wave and the WFAM can be estimated well with the theoretical estimation, especially up to $P_E = O(10^{-1})$. Furthermore, the tails of Wave 6 experiment (Figure 7b) are matching well with the Rayleigh wave height, but Wave 3 (Figure 7a). The tails of the theoretical wave height P_E at $T_p = 1.00$ s underestimate the experimental P_E . The underestimation for the WFAM can be explained by the LTF and coherence findings (Figure 6). From the LTF discussion, Wave 3 has shorter range of high coherence than Wave 6, indicating more pronounced nonlinearity, despite being in the same wave steepness. This consequently results in the underestimation

of the wave height P_E tails with the linear theory in Wave 3. On the other word, having wider linear frequency range in the LTF study provides more similarity of wave height P_E to the Rayleigh P_E , as in Figure 7b. This also demonstrates that the nonlinear dynamics of the WFAM also depends on the diffraction number, for instance between Wave 3 and Wave 6. Wave 3 has higher diffraction number than Wave 6, indicating the importance of nonlinearity interaction in estimating the wave height tail distribution in the large monopile. Nevertheless, the linear theory is still applicable to predict the majority of the wave height distribution.

Deviation from the Rayleigh theory is even more pronounced in the crest distribution. The Rayleigh distribution appears to perform well for the high exceedance probability, $P_E \approx 1.0 - 0.5$, representing low elevations. This is observed at both the incident waves and the WFAM. Corrections to the incident wave tail are available, e.g. Forristall (2000); Gramstad and Lian (2024), meanwhile the nonlinear wave-monopile simulations also observes the tail properties of the WFAM being off from the linear theory (Wang and Low, 2019). They also suggested that the increase of the crest estimation is due to the sum frequencies interactions, which is obviously not captured in the Rayleigh distribution. The underestimation of the crests are also seen in the study of nonlinear runup of the regular waves (Herdayanditya et al., 2022). Furthermore, the findings that linear theory performs better in the wave height than wave crest distributions also appears in different angular and radial positions (Herdayanditya et al., 2024b), although their study only involves $T_p = 1.67$ s.

Correction of the crest distribution of the incident waves based on Forristall (2000) and Gramstad and Lian (2024) are also given in Figure 8. Forristall (2000) requires $m_{0\eta}$ and $m_{1\eta}$ inputs which can be obtained from the JONSWAP spectrum. Meanwhile, Gramstad and Lian (2024) developed a parametrization of the skewness and kurtosis of the incident waves to feed the crest distribution from Tayfun and Fedele (2007). The details of both methods are given in Appendix A. The methods are applied in the present study, which both appear to be better than the Rayleigh distribution. The performance of the distributions from nonlinear waves is also better in Wave 6 than Wave 3. Wave 6 gives good agreement up to $\approx 10^{-2}$. Despite the improvement from Rayleigh distribution, further investigation on the deviation of the observed incident wave crests for the short waves in the Coastal & Ocean Basin shall be performed. This might be caused by the excessive extreme cases near the wave generator or the high frequency cut off in the energy spectrum for the wave maker input, as seen in Tang et al. (2022). It should also be noted that Gramstad and Lian (2024) appears to give better improvement, although still underestimating the experiments. Correction to the WFAM distribution is also performed with the mathematical model of Forristall (2000), where $m_{0\zeta}$ and $m_{1\zeta}$ are used instead, obtained from Eq. (6). It is seen that the correction gives better agreement to the observed WFAM. However, it shall be noted that the WFAM correction is not robust as it was initially derived for the ocean waves, not the WFAM. Therefore, although Corr. 1 works well in Figure 8, it does not perform decently in other locations, resulting in significant value misestimation (discussed in Section 6). An attempt to correct the WFAM crest with Tayfun and Fedele (2007) by feeding the measured skewness and kurtosis from the WFAM time series instead of the parameteric study from Gramstad and Lian (2024) is also performed, but the results are unphysical, possibly because Tayfun and Fedele (2007) was derived for the ocean waves and not for the WFAM.

6 Significant Value Variation

Significant value is usually computed to assess the overall statistics of the WFAM, typically used in engineering analysis. Significant value is the mean of the one-third highest measurements. Figure 9 shows the significant wave height and crest in all the angular positions for the two radial positions. Besides the significant value from the experiments computed with Eq. (14), the theoretical significant value is also shown, computed with Eq. (15a) or Eq. (15b). Corr. 1 distribution in Figure 8 is also employed to correct the linear theory of the significant crest. The correction is based on the practical approach. Knowing that $P_E(\zeta_{Cs}) = \exp(-2)$ for the Rayleigh distribution, the corrected significant crest is then computed from Corr. 1 distribution with the corresponding P_E , identified by Corr. 1.

Figure 9 shows that the WFAM significant height can be predicted well with the linear theory via spectral analysis. Furthermore, the linear theory performance is decent in both of the peak periods and all the measurement positions. It is interesting to see that despite the tail difference observed in the wave height of the WFAM at the Wave 3 (Figure 7a), the significant value appears to agree decently with the linear theory (Figure 9a and Figure 9b). Similarly, the tail of Wave 6 (Figure 7b) results in good agreement of significant wave height between the linear theory and the physical experiments (Figure 9c and Figure 9d). Moreover, the WFAM significant height also appears to be not sensitive to the incident wave steepness (Wave 1 - Wave 3 and Wave 4 - Wave 6 in Figure 9). Meanwhile, the WFAM significant crests around the monopile is observed to deviate from the linear theory in the investigated points. This is in agreement with the discussion of Figure 8, in which the crest properties deviate further from the linear theory than the wave height properties. Furthermore, the magnitude of the significant crest is also sensitive to the incident wave steepness. On

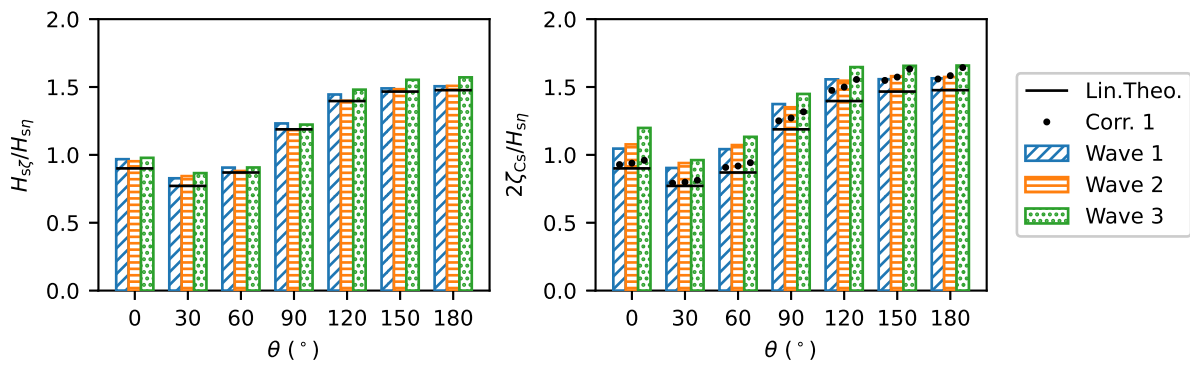
the other hand, the corrected significant crest appears to give closer estimation to the physical experiments, especially at the upwave part. The downwave part from the corrected value still shows noticeable deviation with the physical experiment, especially at $r/R = 1.5$. It is also seen that the corrected values even overestimate the value of the highest incident wave steepness for $T_p = 1.67$ s at $r/R = 1.5$; $\theta = 30^\circ$ and $\theta = 60^\circ$. These misestimations also demonstrate the unrobustness of the corrected method.

Generally, larger incident wave steepness gives larger significant crest elevation in all the measurement points. The general increase of the value in the increasing incident wave steepness is also captured with the corrected value. However, at $r/R = 1.5$; $\theta = 30^\circ$ and $\theta = 60^\circ$ of $T_p = 1.67$ s, it is the opposite, making the corrected value overestimate the physical experiments. This can be explained by Wave Type II breaking phenomena. Wave Type II will also be elaborated to explain the high crest occurrence that occur in the downwave side of the monopile ($\theta = 0^\circ$). For instance, in Figure 9a and Figure 9c, the crest significant value at $\theta = 0^\circ$ deviates the furthest from the linear theory and the correction method also fails to capture it, despite good agreement observation in the wave height significant value.

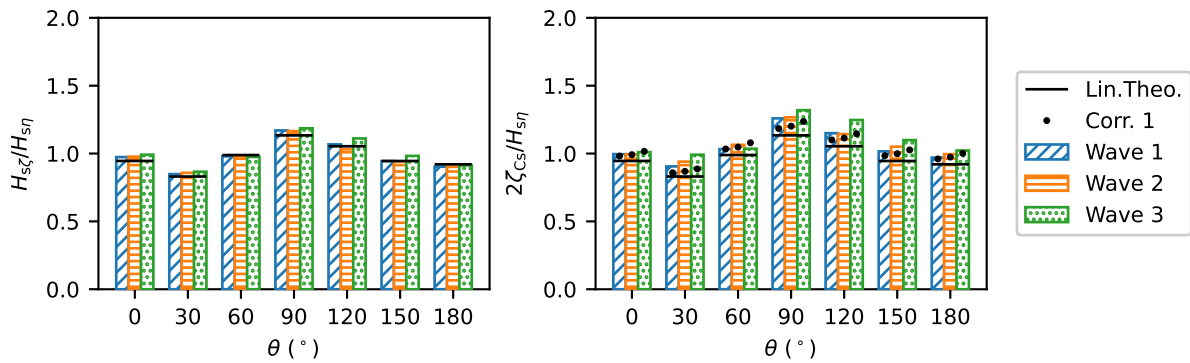
When regular waves hit a monopile, there are Wave Type I that travels cocentrally due to the wash up-down at the vicinity of the upwave and downwave of the monopile and Wave Type II that travels clockwise and anti-clockwise around the monopile. This is explained by Swan and Sheikh (2015) from a series of regular wave experiments. Previously, the observation of waves travelling around the monopile has also been similarly seen when moving the cylinder in the still water condition (Retzler et al., 2000), although it is unable to explain the recirculation observed in the fixed cylinder with long incident waves. Wave Type I and Type II are nonlinear wave behaviours that can only be captured with nonlinear free surface solvers in either potential flow (Christou, 2009) or Navier Stokes (Sun et al., 2016; Mohseni et al., 2018) solvers. Thus, it is missing in the Rayleigh estimation. The sequence of the observed Wave Type I and Type II in regular incident waves can be described in the following:

1. When the regular wave crest hits the upwave side of the monopile, a lump of water is created.
2. As the regular wave crest travels to the backside of the monopile, the lump of water at the front side of the monopile is wash-down, creating cocentric waves at the upwave side of the monopile, defined as Wave Type I.
3. When the crest is travelling to the downwave side, edge waves are also travelling along with the crest, on one side moving clockwise and on the other side moving counter-clockwise. In Mohseni et al. (2018), they described them as edge waves while Swan and Sheikh (2015); Sun et al. (2016) described them as Wave Type II.
4. Afterwards, the incident crest arrives at the downwave side of the monopile, from which the Wave Type II, collapse to each others.
5. As the next phase, the water velocity is in the opposite direction of the wave propagation, creating the same phenomena but with the opposite direction (i.e. Wave Type I is formed at the downwave side and the Wave Type II travels to the opposite of wave propagation and collapse at the upwave part of the monopile). However, the strength of the Wave Type II collision in the upwave side depends on the wave and cylinder properties (Mohseni et al., 2018).

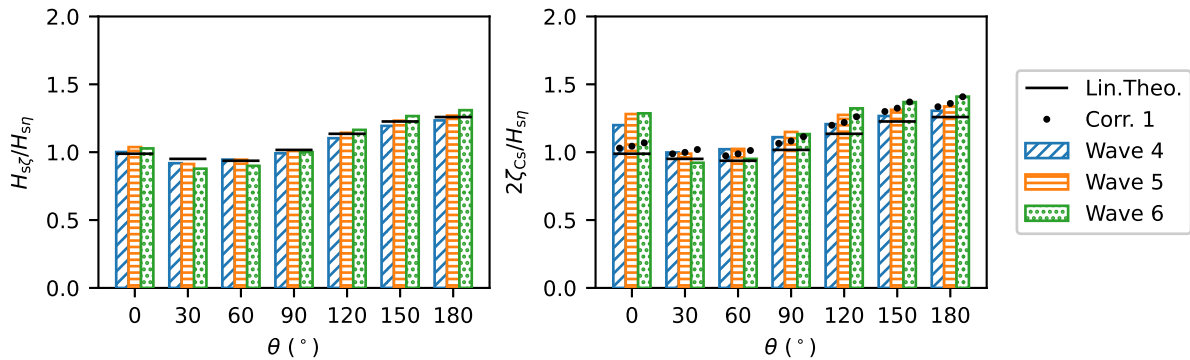
Wave Type II also appears in the present experiments where irregular waves are employed. An example of Wave Type II is shown in Figure 10, although it is broken. The snapshot consists of snapshot of waterlump initialization, Figure 10a, followed by unstable and broken waves in Figure 10b and Figure 10c. Besides the broken Wave Type II (Figure 10), there also exists the unbroken Wave Type II that embedded in the total WFAM. Wave Type II travels around the monopile and collides at the downwave side of the monopile, which gives the explanation of large crest occurrence in the downwave of Figure 9a and Figure 9c. Further, when the Wave Type II increases, the stability of the waves decrease and cause breaking waves, thus the significant value of $\theta = 30^\circ$ and $\theta = 60^\circ$ of $T_p = 1.67$ s gets lower in increasing steepness. In order to elaborate further, the crest exceedance probability of three locations are shown in Figure 11, zoomed in on the one-third highest value which defines the significant value of the crests. In the upwave ($\theta = 180^\circ$), Wave 3 and Wave 6 exceedance probability are higher than the other less nonlinear waves in the respective periods. As seen in the Figure 10a, there is a lump of water in front of the monopile, due to Wave Type I and Wave Type II. This lump of water, therefore, gets larger in increasing incident wave steepness, causing higher crest at $\theta = 180^\circ$. However, at the $\theta = 60^\circ$, the highest nonlinear waves does not necessarily gives the highest crests. The tails of Wave 3 and Wave 5 appears to be bended resulting lower P_E than the less steep waves, Wave 2 and Wave 4 in turn. The bended shape of P_E is a typical shape of broken waves (Karpadakis and Swan, 2022). Furthermore, Wave 6 does not show bended shape, but the P_E is lower than the other less steep waves, indicating that the breaking phenomena is more severe. Afterwards, Wave Type II that travels clockwise and anti-clockwise collapses again at the $\theta = 0^\circ$ resulting the deviation of exceedance probability of the crest to the linear theory. Despite the observed broken waves, the impact on the significant value wave height is not significant as seen in Figure 11. This can be explained



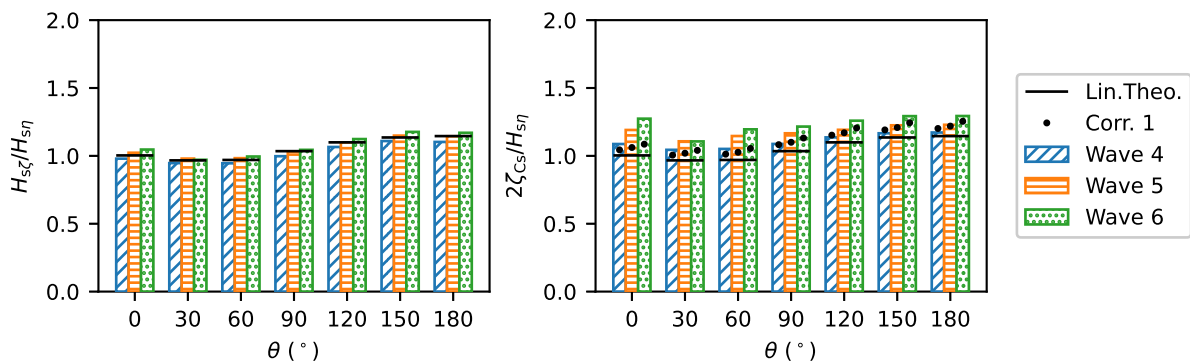
(a) Significant Value of the WFAM height (left) and crest (right) of $T_p = 1.00$ s at $r = 1.5R$



(b) Significant Value of the WFAM height (left) and crest (right) of $T_p = 1.00$ s at $r = 3R$



(c) Significant Value of the WFAM height (left) and crest (right) of $T_p = 1.67$ s at $r = 1.5R$



(d) Significant Value of the WFAM height (left) and crest (right) of $T_p = 1.67$ s at $r = 3R$

Figure 9: The comparison between the physical experiment significant values and the theoretical significant values. Significant wave height and significant crest are computed.

by the fact that the breaking waves only occur at the low exceedance probability, thus the average of the one-third highest value are relatively similar.

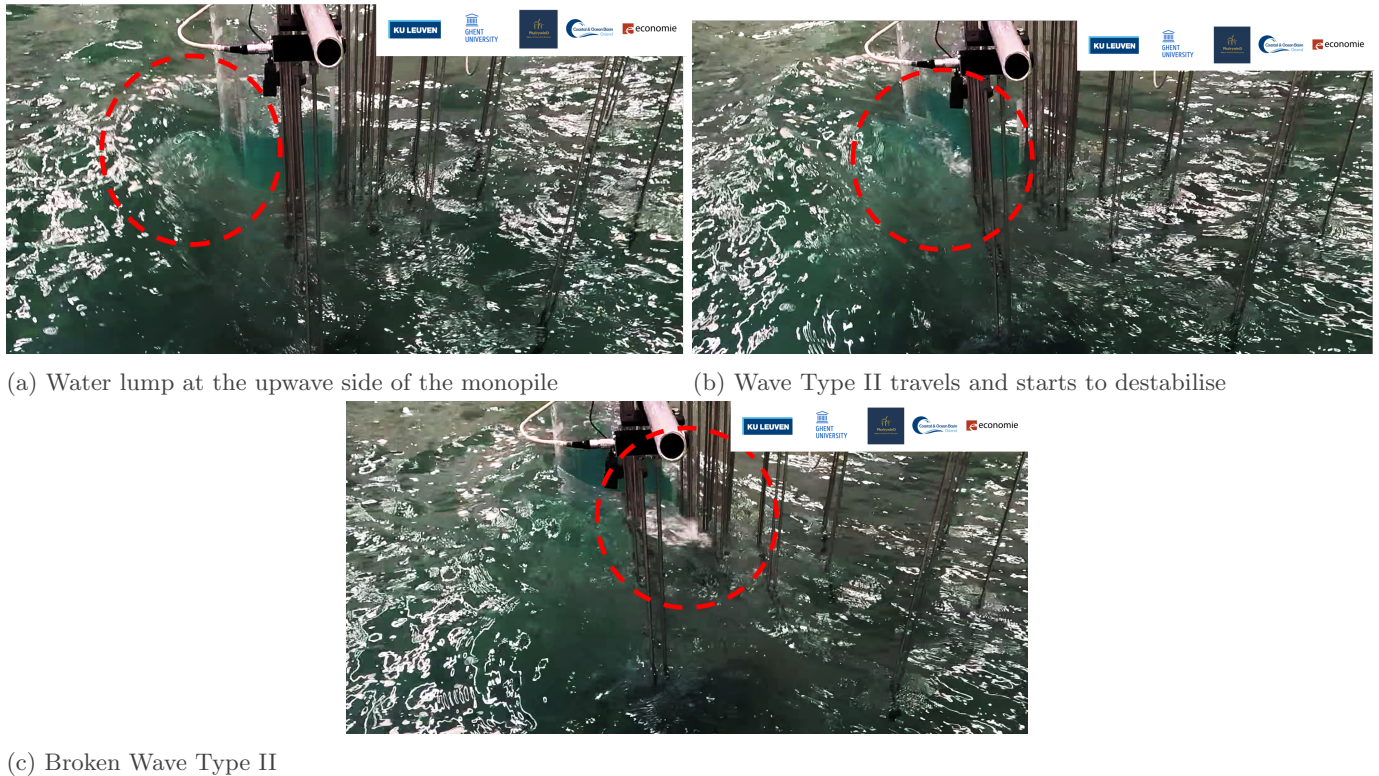


Figure 10: Snapshot of broken Wave Type II from Wave 6. The evolution of the Wave Type II is identified with red circle. Wave Type II is wave that travels around the monopile in clockwise and anti-clockwise that collides at the downwave side.

The crest misestimation in locations around the monopile can be improved with more advanced analytical/numerical solutions or more robust distribution correction obtained through parametric study. The former would require the capability to capture the breaking waves, as observed in the present study despite moderate incident wave steepness. Since, the advanced solvers take a large computational time, it might not be suitable to the marine operation plannings, making the distribution correction more preferable. The correction for the WFAM distribution would require WFAM in various wave steepness and/or wave diffraction number. The parametric equation approach has also been applied to improve the crest nonlinearity, by mean of fitting the observations to the Weibull distribution for the ocean waves (e.g. Forristall, 2000) or the wave field at sloped beach (e.g. Xu et al., 2021). This approach can similarly be performed to correct the WFAM crest. In that way, the Wave Type II and the tail breaking waves are also accounted for, rather than relying on the open-ocean crest correction.

7 Conclusions

Monopile diameter has increased significantly in the recent years, posing a new challenge to safe marine operation plannings. When the monopile size is small, it is acceptable to neglect the monopile for marine operability analysis, but not for the large monopiles. In the present study, the effect of the monopile on the WFAM is investigated via physical experiments that were performed in The Coastal & Ocean Basin, Ostend. Six long crested irregular waves were simulated to investigate the WFAM in two diffraction numbers and two wave steepness. Initially, the Linear Transfer Function (LTF) of the monopile is evaluated. It is found that the LTF matches the linear theory within the frequency of the notable incident wave energy. It is also found that the frequency range of the good agreement becomes less in the large monopile case. Consequently, the exceedance probability of the wave height around the large monopile slightly deviates from the linear theory. The nonlinear effect is even more pronounced in the crest properties of the WFAM.

Significant value of the WFAM height and crest are computed as it is typically employed in ocean engineering analysis. Despite the slight tail difference in WFAM height to the linear theory, the significant value of the WFAM height are predicted well with linear theory, but the WFAM crest deviates from the linear theory. Present study also introduces a practical correction method based on the ocean crest distribution. It appears to performs well in the

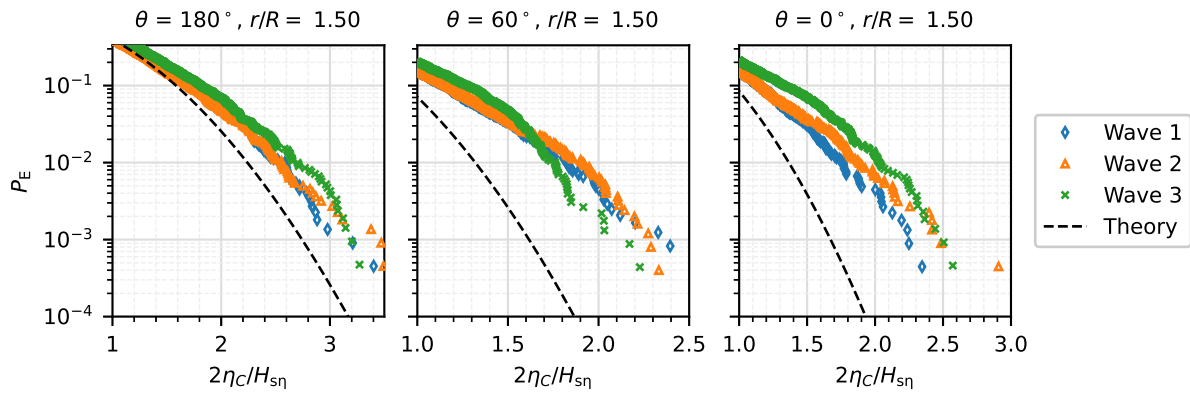
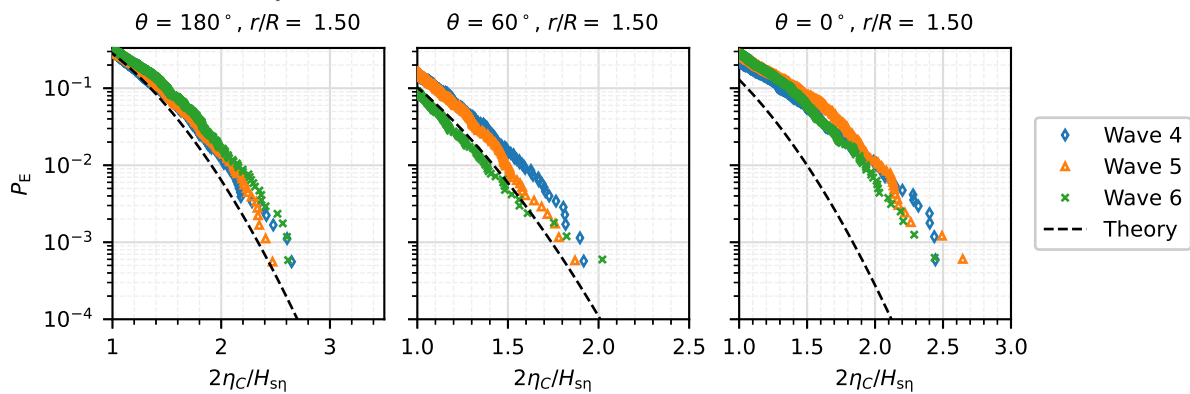

 (a) LTF from Wave 1 - 3, with $T_p = 1.00$ s

 (b) LTF from Wave 4 - 6, with $T_p = 1.67$ s

Figure 11: The significant value comparison between the physical experiments and the theoretical.

upwave part but not in the downwave part. The crests are driven by the nonlinear effect in Wave Type I or Wave Type II. Therefore, the practical solution accuracy also depends on the evolution of the Wave Type II. At region where the Wave Type II collapse, in the present study on the downwave side, the practical correction method performs the worst. Furthermore, it has been demonstrated as well that broken Wave Type II can also cause lower tail crest distribution than the less steepness incident waves. This seems to also cause the correction method to overestimate the observed significant value in some locations. Nevertheless, provided that the wave height information is needed for a marine operation, linear theory can be used, for instance, to feed the wave field information for anode-cage installation or fallpipe operation analysis around a monopile. Meanwhile, if the marine operation is more sensitive to the wave crest information, the linear theory is not sufficient, for instance, deck wetness during the crew transfer operation at the boat landing. In the condition where fast computation with better accuracy than linear theory in the crest elevation estimation is needed, the correction method can be utilised on the fly, along with its limitation to capture the Wave Type II collision and breaking phenomena. It is also a recommendation to the marine operation planning that broken waves might be seen around the monopile. From this study, the breaking waves at tail of the wave distribution is already seen in the range $\frac{1}{2}k_p H_s = 0.10 - 0.15$ although the order of magnitude differs in different period. While the breaking condition can be defined via breaker index in the coastal environment, the quantification of the breaking waves limit around the monopile is not clear yet, requiring further investigation.

Acknowledgements

We acknowledge the financial support from the Energy Transition Fund (ETF) of the Belgian Federal Government (FPS Economy) within PhairywinD Project and the cooperation with the Coastal & Ocean Basin, Ostend to perform the physical experiments.

Funding

This work has been funded by the Energy Transition Fund (ETF) of the Belgian Federal Government (FPS Economy) within PhairywinD Project.

Author contributions (CRediT)

IH: Writing-original draft, Formal analysis, Project planning, Visualization, Manuscript Draft Review; MS: Manuscript draft review and editing, Project planning; EL: Manuscript draft review and editing, Conceptualization, Supervision; PR: Manuscript draft review and editing, Conceptualization, Supervision.

Data access statement

The data acquired in the study will be made available upon request.

Declaration of interest

There is no conflict of interest.

References

- Ancellin, M. and Dias, F. (2019). Capytaine: a python-based linear potential flow solver. *Journal of Open Source Software*, **4**(36), 1341.
- Andersen, T.L., Frigaard, P., Damsgaard, M. and De Vos, L. (2011). Wave run-up on slender piles in design conditions—model tests and design rules for offshore wind. *Coastal Engineering*, **58**(4), 281–289.
- Babarit, A. and Delhommeau, G. (2015). Theoretical and numerical aspects of the open source bem solver nemoh, In: *11th European wave and tidal energy conference (EWTEC2015)*.
- Büchmann, B., Skourup, J. and Kriebel, D.L. (1999). Second order wave interaction with a large structure, In: *Coastal Engineering 1998*, 1613–1624.
- Chau, F. and Taylor, R.E. (1992). Second-order wave diffraction by a vertical cylinder. *Journal of Fluid Mechanics*, **240**, 571–599.
- Christou, M. (2009). *Fully nonlinear computations of waves and wave-structure interaction*, Ph.D. thesis, Department of Civil and Environmental Engineering, Imperial College London.
- Dalzell, J. (1976). Application of the functional polynomial model to the ship added resistance problem, In: *Published by Stevens institute of Technology, 11th Symposium on Naval Hydrodynamics, London, UK*.
- De Vos, L., Frigaard, P. and De Rouck, J. (2007). Wave run-up on cylindrical and cone shaped foundations for offshore wind turbines. *Coastal Engineering*, **54**(1), 17–29.
- Ferrant, P., Malenica, Š. and Molin, B. (1999). Nonlinear wave loads and runup on a vertical cylinder, In: *Nonlinear water wave interaction*, Advances in Fluid Mechanics, Computational Mechanics Publications.
- Forristall, G.Z. (2000). Wave crest distributions: Observations and second-order theory. *Journal of physical oceanography*, **30**(8), 1931–1943.
- Gaertner, E., Rinker, J., Sethuraman, L., Zahle, F., Anderson, B., Barter, G.E., Abbas, N.J., Meng, F., Bortolotti, P., Skrzypinski, W. et al. (2020). Iea wind tcp task 37: definition of the iea 15-megawatt offshore reference wind turbine, Technical report, National Renewable Energy Lab.(NREL), Golden, CO (United States).
- Gramstad, O. and Lian, G. (2024). Parametrization of sea surface skewness and kurtosis with application to crest distributions. *Journal of Fluid Mechanics*, **979**, A4. DOI:10.1017/jfm.2023.1047.

- GWEC, G.W.E. (2023). Global wind report 2023.
- Hallermeier, R.J. (1976). Nonlinear flow of wave crests past a thin pile. *Journal of the Waterways, Harbors and Coastal Engineering Division*, **102**(4), 365–377.
- Herdayanditya, I., Baert, B., Stempinski, F., Rauwoens, P. and Lataire, E. (2024a). Application of irregular frequency removal feature in capytaine for anode cage installation over a monopile wind turbine, In: *International Conference on Offshore Mechanics and Arctic Engineering*, volume 87820, V05AT06A063, American Society of Mechanical Engineers.
- Herdayanditya, I., Rauwoens, P., Fernandez, G.V., Martínez-Estévez, I. and Lataire, E. (2022). Monopile run-up study using eulerian and lagrangian numerical models. *Trends in Renewable Energies Offshore*, 491–499.
- Herdayanditya, I., Streichers, M., Lataire, E. and Rauwoens, P. (2024b). Experimental study of the wave field around a monopile due to moderate steepness irregular incident waves. *CoastLab 2024: Physical Modelling in Coastal Engineering and Science*.
- Ji, X., Liu, S., Li, J. and Jia, W. (2017). Numerical investigation of multidirectional random wave interaction with a large cylinder. *Proceedings of the Institution of Mechanical Engineers, Part M: Journal of Engineering for the Maritime Environment*, **231**(1), 271–283.
- Jiang, C. and el Moctar, O. (2022). Numerical investigation of wave-induced loads on an offshore monopile using a viscous and a potential-flow solver. *Journal of Ocean Engineering and Marine Energy*, **8**(3), 381–397.
- Karmpadakis, I. and Swan, C. (2022). A new crest height distribution for nonlinear and breaking waves in varying water depths. *Ocean Engineering*, **266**, 112972.
- Kim, C. (2008). *Nonlinear Waves and Offshore Structures*, World Scientific.
- Kim, M.H. and Yue, D.K. (1990). The complete second-order diffraction solution for an axisymmetric body part 2. bichromatic incident waves and body motions. *Journal of Fluid Mechanics*, **211**, 557–593.
- Kim, N. and Kim, C.H. (2005). Surge motion of mini tlp in random seas-comparison between experiment and theory, In: *ISOPE International Ocean and Polar Engineering Conference*, ISOPE-I, ISOPE.
- Kriebel, D. (1990). Nonlinear wave interaction with a vertical circular cylinder. part i: Diffraction theory. *Ocean Engineering*, **17**(4), 345–377.
- Kriebel, D.L. (1992). Nonlinear wave interaction with a vertical circular cylinder. part ii: Wave run-up.
- Lin, Z., Qian, L., Bai, W., Ma, Z., Chen, H., Zhou, J.G. and Gu, H. (2021). A finite volume based fully nonlinear potential flow model for water wave problems. *Applied Ocean Research*, **106**, 102445.
- Liu, S., Gatin, I., Obhrai, C., Ong, M.C. and Jasak, H. (2019). Cfd simulations of violent breaking wave impacts on a vertical wall using a two-phase compressible solver. *Coastal Engineering*, **154**, 103564.
- MacCamy, R. and Fuchs, R.A. (1954). *Wave forces on piles: a diffraction theory*, 69, US Beach Erosion Board.
- Mohseni, M., Esperanca, P.T. and Sphaier, S.H. (2018). Numerical study of wave run-up on a fixed and vertical surface-piercing cylinder subjected to regular, non-breaking waves using openfoam. *Applied Ocean Research*, **79**, 228–252.
- Molin, B. et al. (1995). Third-harmonic wave diffraction by a vertical cylinder. *Journal of Fluid Mechanics*, **302**, 203–229.
- Morris-Thomas, M. and Thiagarajan, K. (2004). The run-up on a cylinder in progressive surface gravity waves: harmonic components. *Applied Ocean Research*, **26**(3-4), 98–113.
- Negro, V., López-Gutiérrez, J.S., Esteban, M.D., Alberdi, P., Imaz, M. and Serraclara, J.M. (2017). Monopiles in offshore wind: Preliminary estimate of main dimensions. *Ocean Engineering*, **133**, 253–261.
- Niedzwecki, J.M. and Duggal, A.S. (1992). Wave runup and forces on cylinders in regular and random waves. *Journal of waterway, port, coastal, and ocean engineering*, **118**(6), 615–634.
- Ramirez, J., Frigaard, P., Andersen, T.L. and de Vos, L. (2013). Large scale model test investigation on wave run-up in irregular waves at slender piles. *Coastal Engineering*, **72**, 69–79.

- Ramirez, L., Fraile, D. and Brindley, G. (2020). Offshore wind in europe: Key trends and statistics 2019.
- Retzler, C., Chaplin, J. and Rainey, R. (2000). Transient motion of a vertical cylinder: measurements and computations of the free surface. *Water Waves and Floating Bodies*, 154.
- Sharma, J. and Dean, R. (1981). Second-order directional seas and associated wave forces. *Society of Petroleum Engineers Journal*, **21**(01), 129–140.
- Sibetheros, I., Niedzwecki, J. and Teigen, P. (2005). Analysis of wave run-up measurements on a mini-tlp, In: *International Conference on Offshore Mechanics and Arctic Engineering*, volume 41952, 881–890.
- Sun, L., Zang, J., Chen, L., Taylor, R.E. and Taylor, P. (2016). Regular waves onto a truncated circular column: A comparison of experiments and simulations. *Applied ocean research*, **59**, 650–662.
- Swan, C. and Sheikh, R. (2015). The interaction between steep waves and a surface-piercing column. *Philosophical Transactions of the Royal Society A: Mathematical, Physical and Engineering Sciences*, **373**(2033), 20140114.
- Tang, T., Barratt, D., Bingham, H.B., van den Bremer, T.S. and Adcock, T.A. (2022). The impact of removing the high-frequency spectral tail on rogue wave statistics. *Journal of Fluid Mechanics*, **953**, A9.
- Tayfun, M.A. and Fedele, F. (2007). Wave-height distributions and nonlinear effects. *Ocean engineering*, **34**(11-12), 1631–1649.
- Taylor, R.E. and Huang, J. (1997). Semi-analytical formulation for second-order diffraction by a vertical cylinder in bichromatic waves. *Journal of fluids and structures*, **11**(5), 465–484.
- UN (2015). Transforming our world: the 2030 agenda for sustainable development. *UN Doc. A/RES/70/1 (September 25, 2015)*.
- Wang, Z. and Low, Y.M. (2019). Analysis of the extreme wave elevation due to second-order diffraction around a vertical cylinder. *Applied Ocean Research*, **86**, 222–238.
- Xu, J., Liu, S., Li, J. and Jia, W. (2021). Experimental study of wave height, crest, and trough distributions of directional irregular waves on a slope. *Ocean Engineering*, **242**, 110136.
- Young, I. (1995). The determination of confidence limits associated with estimates of the spectral peak frequency. *Ocean engineering*, **22**(7), 669–686.
- Zelt, J. and Skjelbreia, J.E. (1992). Estimating incident and reflected wave fields using an arbitrary number of wave gauges, In: *Coastal Engineering 1992*, 777–789.

Appendix

A Nonlinear Crest Distribution

A.1 Crest distribution according to Forristall (2000)

The crest distribution from Forristall (2000) is derived from the parametric study of their second-order wave simulations based on the second-order solution of Sharma and Dean (1981). The parametric study employs Weibull Distribution, Eq. (16). α and β are assumed to be equal to Rayleigh distribution when the irregular waves have zero steepness, Eq. (17a) and Ursell number, Eq. (17b), where T_1 and k_1 are the mean period and its corresponding wave number. The mean period can be computed with $m_{0\eta}$ and $m_{1\eta}$ information. They found that α, β for the long crested waves (α_2, β_2) are as in Eqs. (18) and for the short crested waves (α_3, β_3) are as in Eqs. (19).

$$P_E(\eta_C) = \exp \left[- \left(\frac{\eta_C}{\alpha H_{s\eta}} \right)^\beta \right] \quad (16)$$

$$S_1 = \frac{2\pi H_{s\eta}}{gT_1^2} \quad (17a)$$

$$Ur = \frac{H_{s\eta}}{k_1^2 h^3} \quad (17b)$$

$$\alpha_2 = 0.3536 + 0.2892S_1 + 0.1060Ur \quad (18a)$$

$$\beta_2 = 2 - 2.1597S_1 + 0.0968Ur^2 \quad (18b)$$

$$\alpha_3 = 0.3536 + 0.2568S_1 + 0.0800Ur \quad (19a)$$

$$\beta_3 = 2 - 1.7912S_1 - 0.5302Ur + 0.284Ur^2 \quad (19b)$$

A.2 Crest distribution according to Gramstad and Lian (2024)

Gramstad and Lian (2024) derived a parametric equations, Eqs (20) to describe skewness, S_η , and kurtosis, K_η of the nonlinear irregular waves based on their nondimensional steepness (ϵ), nondimensional dispersion (ξ), nondimensional peak parameter (ν), and nondimensional spread (τ) parameters described in Eqs. (21) where σ_θ is spreading standard deviation. They used their parametric S_η and K_η to feed Tayfun and Fedele (2007) crest distribution, described in Eq. (22), where χ is a solution of Eq. (23).

$$S_\eta = (2.89 + 1.19\xi^{3.3} - 0.28\nu^{0.8} + 0.35\xi^{2.9}\nu^{1.1}) (1 + 1.42\tau - 3.81\tau^2 + 2.25\tau^3) \epsilon \quad (20a)$$

$$K_\eta = (2.34 - 0.31\xi) S_\eta^2 \quad (20b)$$

$$\epsilon = k_p \sqrt{m_0} \quad (21a)$$

$$\xi = (k_p h)^{-1} \quad (21b)$$

$$\nu = \ln(\gamma) \quad (21c)$$

$$\tau = \sin(\sigma_\theta) \quad (21d)$$

$$P_E \left(\frac{\eta_C}{H_{s\eta}} \right) = \exp(-8\chi^2) \left\{ 1 + \frac{8}{3} K_\eta \left(\frac{\eta_C}{H_{s\eta}} \right)^2 \left[4 \left(\frac{\eta_C}{H_{s\eta}} \right)^2 - 1 \right] \right\} \quad (22)$$

$$\frac{\eta_C}{H_{s\eta}} = \chi + 2S_\eta \frac{\chi^2}{3} \quad (23)$$